https://doi.org/10.5194/egusphere-2026-2920
Preprint. Discussion started: 12 June 2026

Simulating enhanced ocean alkalinity experiments in a high-latitude fjord using nested ROMS simulations coupled with MARBL biogeochemistry

Ulla K. Heede[1], Matthew C. Long[1], Alicia Karspeck[1], Scott Bachman[1], Nora Loose[1], Dafydd Stephenson[1], David T. Ho[2], Lennart Gerke[1], Tobias Koffman[2], Alice Benoit-Cattin[3]; Sara Harðardóttir[3], and Andreas Macrander[3]

[1][C]Worthy, Boulder, Colorado, USA
[2]Department of Oceanography, University of Hawai'i at Mānoa, Honolulu, Hawaii, USA
[3]Marine and Freshwater Research Institute (MFRI), Hafnarfjörður, Iceland

Correspondence to: Ulla K. Heede, 1909 Broadway Ste 200, Boulder, CO 80302, USA, ulla@cworthy.org.

Abstract. Ocean-based carbon dioxide removal (CDR) technologies have the potential to make significant contributions to climate change mitigation, yet more research is needed to deepen our understanding of their effectiveness and safety. One proposed method, ocean alkalinity enhancement (OAE), involves increasing seawater alkalinity to promote additional carbon uptake and long-term storage in the ocean. Ocean models are crucial tools to accompany OAE field trials and research, as alkalinity signals are rapidly diluted, and observations alone cannot capture the spatiotemporal scales at which interventions evolve. The C-Star open source regional ocean-biogeochemical modeling system is designed to support OAE research and quantification. Here, we present results from deploying C-Star in a nested regional modeling configuration established for Hvalfjörður, a fjord located in western Iceland. We compare the model solution with observations collected during a 2024 field campaign. These include repeated measurements of the fjord's physical and chemical state, as well as a tracer release and sampling program used to assess the model's ability to reproduce tracer transport and dispersal. We find that the model captures key features of the circulation in the fjord, including tidally driven currents and sea-surface height variations, tracer dispersal, and seasonal stratification. Next, we use C-Star to simulate six 96 hr OAE releases in the fjord under varying seasonal, tidal, and weather conditions. The OAE experiments produce a ~1 km^2 plume with detectable anomalies in alkalinity, pH and pCO_2 during the release. The uptake of CO_2 from the atmosphere is 0.05 to 0.15 mol of carbon absorbed per mol of added alkalinity during and four days following the release, and surface winds and seasonal stratification are key for both alkalinity dispersal and air-sea gas exchange. The model exhibits background biases in alkalinity, dissolved inorganic carbon (DIC), and nutrients, arising from limitations in initial and boundary conditions and representation of in situ biogeochemical processes. While these biases are a target for improvement, we show that they do not significantly degrade the model's ability to simulate OAE-relevant anomalies. Overall, this work enhances confidence in the applicability of C-Star nested model domains as OAE research and field-trial support tools in fjord and estuary systems.

https://doi.org/10.5194/egusphere-2026-2920
Preprint. Discussion started: 12 June 2026

1 Introduction

The ocean plays a central role in the global carbon cycle as the largest active carbon reservoir on Earth, and the ultimate long-term reservoir for most of the transient carbon released to the atmosphere (Sarmiento and Gruber 2006). Since the industrial revolution, the ocean has absorbed approximately 25–30% of anthropogenic carbon dioxide (CO_2) emissions, thereby mitigating the pace of climate change (Gruber et al. 2019; Friedlingstein et al. 2026). Yet, as atmospheric CO_2 continues to rise, consensus assessments (Bashmakov et al. 2022) indicate that achieving international warming targets will require large-scale carbon dioxide removal (CDR), prompting increasing interest in deliberately enhancing the ocean's role as a carbon sink. Ocean-based CDR approaches encompass a range of techniques, from ocean alkalinity enhancement (OAE) to biomass-based interventions; each of these approaches aims to accelerate the transfer of carbon from the atmosphere into long-lived oceanic reservoirs (Ho and Bopp 2024). While ocean-based CDR has the potential to contribute significantly to climate change mitigation portfolios, it also raises important scientific, environmental, and governance challenges, given uncertainties in efficacy, monitoring, and potential ecological side effects (National Academies 2022).

One of the central challenges in deploying marine CDR is quantifying CO_2 uptake owing to a particular intervention in the ocean. For example, in the case of OAE, dispersion by ocean currents and turbulence, varying rates of ocean-atmosphere gas exchange, and biogeochemical feedbacks can strongly influence both the persistence and spatial footprint of added alkalinity, as well as its ultimate effectiveness in enhancing carbon uptake (Liu et al. 2025; Zhou et al. 2025). Directly observing these processes in open water is logistically difficult and costly, requiring a combination of in situ measurements, autonomous platforms, and remote sensing (Fennel 2025). Further, as material is diluted and transported away from release locations, the OAE signals become very small relative to background fields and their variability. Because of this, robust and validated ocean biogeochemical models are indispensable tools for simulating the effects of ocean-based CDR interventions.

Beyond monitoring and verification, ocean circulation and biogeochemical models are also crucial in the planning and permitting stages of marine CDR field trials and research. High-resolution regional models allow researchers to evaluate how site-specific conditions, such as tidal regimes, water column stratification and weather patterns, influence the dispersion and dilution of added materials (e.g., alkalinity), thereby informing safe and effective deployment strategies (Laurent et al. 2026). In the case of OAE, models can simulate the spatiotemporal evolution of changes in pH and carbonate saturation states owing to the alkalinity addition, thus suggesting safe and effective study designs (Paul et al. 2025). Model results can further guide the placement of observational assets, ensuring that measurements can capture both the intended signal and potential unintended consequences. In this way, validated high-resolution modeling frameworks can serve as decision-support tools for designing CDR field trials.

https://doi.org/10.5194/egusphere-2026-2920
Preprint. Discussion started: 12 June 2026

The C-Star platform, developed by [C]Worthy, is a community-oriented ocean modeling framework explicitly tailored to support CDR research and applications (Lippiatt, 2025). It is engineered to simplify the setup and execution of regional ocean modeling experiments that integrate ocean biogeochemistry, tracers, and CDR modules while ensuring scientific rigor and reproducibility (C-Star Documentation, 2026). In doing so, C-Star fills a critical methodological gap in marine CDR research, offering a reproducible and accessible modeling infrastructure (He, 2024).

The goal of this study is to use C-Star nested regional ocean modeling capabilities to simulate the background flow and carbonate system in Hvalfjörður, Iceland, to evaluate the model solution against observational data, and to simulate potential OAE deployments in the fjord. By establishing this modeling domain, we provide a demonstration of the technical feasibility of configuring high-resolution regional ocean-biogeochemical models with C-Star and establish the model as a tool for supporting future carbon cycle and CDR research in Hvalfjörður. Note that in this study, we focus on the near-field (defined as the extent of Hvalfjörður, see site description in section 2.1) detectability and carbon uptake for the purpose of providing insights on a deployment-relevant scale, and the aim is not to calculate the total carbon uptake from a given CDR intervention for which a larger ocean domain would be required.

The remainder of this manuscript is organized as follows. In Section 2, we detail the model configuration and inputs, and provide a description of the Hvalfjörður study site. This section also characterizes the observational datasets used for model evaluation, the specifics of a dual-tracer release field experiment, and the experimental design for both dye tracer and OAE simulations. Section 3 begins with a model–observation comparison, including an evaluation of the model mean state, seasonal evolution, and tracer dispersal. It then presents the results of the OAE ensemble simulations, focusing on signal detectability, pH excursions, and CO_2 uptake efficiency. Finally, Section 4 summarizes the core findings, discusses the implications for future field trial planning and identifies key avenues for the continued development of the model solution.

2 Methods

2.1 Site description

Hvalfjörður is a fjord located in Faxaflói Bay in southwest Iceland, approximately 30 km north of Reykjavík (Fig. 1a). The fjord extends about 35 km inland from the coast, with a width of 4–5 km, and depths ranging from ~5 m in the inner fjord to ~40 m in the outer fjord with a maximum depth of 83 m (Fig. 1b). The tidal regime is semi-diurnal, with typical tidal ranges of 1.5 to 4.5 m. The time-mean circulation pattern is counter-clockwise, characterized by inflow of water at depth, mostly along the southern margin of the fjord, and compensating surface outflow along the northern side, consistent with estuarine-type circulation observed in other Icelandic fjords (Macrander et al. 2021). Several small rivers and streams flow into Hvalfjörður, contributing freshwater inputs that influence the fjord's stratification and biogeochemistry. Among the largest

https://doi.org/10.5194/egusphere-2026-2920
Preprint. Discussion started: 12 June 2026

95 rivers are Laxá í Kjós on the south side and Brynjudalsá and Botnsá in the inner fjord, draining surrounding mountain catchments and valleys.

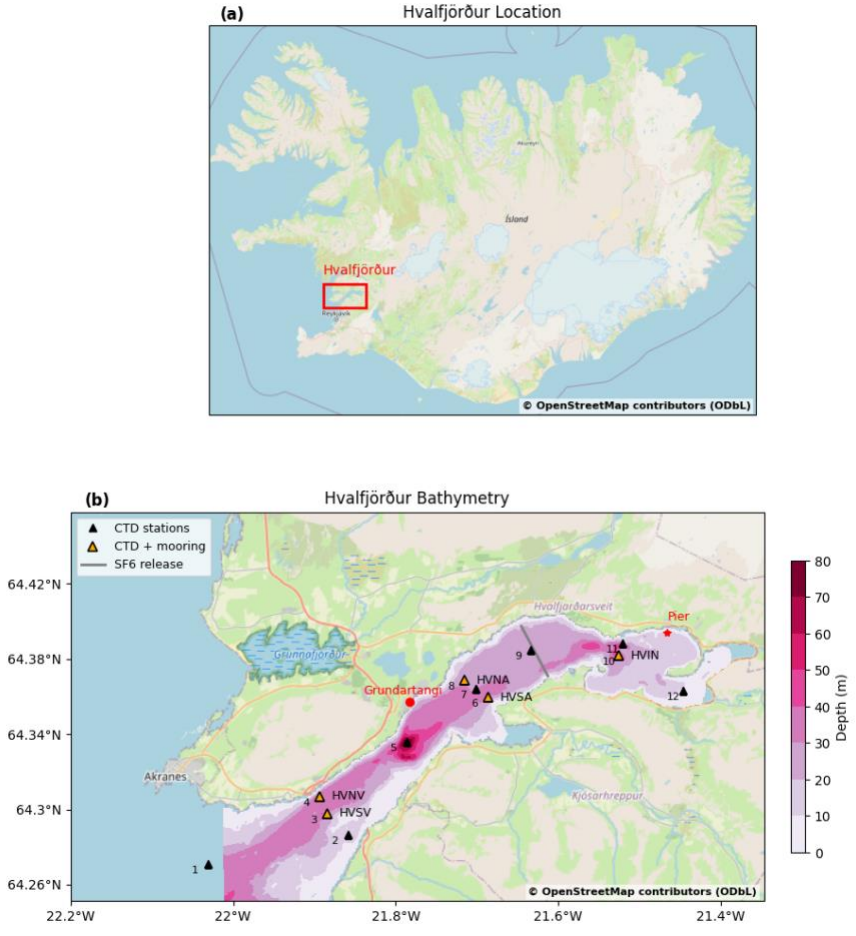

Figure 1: Field-site overview with a) the location of Hvalfjörður in Iceland, and b) the bathymetry in the fjord from the EMOD
100 **bathymetry dataset used in the model setup (see section 2.2) as well as the location of CTD stations and moorings (section 2.3), and the release location of the tracers during the dual-tracer experiment (section 2.4). The Grundartangi tidal gauge station is marked, as well as the pier, which is the alkalinity release location for the modeled OAE experiments.**

The region experiences a subpolar oceanic climate, with mean annual air temperatures ranging from approximately −1°C in
105 winter to 12°C in summer, and precipitation of 80-120 mm per month. Winds in Hvalfjörður are strongly influenced by synoptic weather patterns over the North Atlantic, with varying wind directions, and typical near-surface speeds of 5–10 m s^{-1} (Icelandic Meteorological Office).

https://doi.org/10.5194/egusphere-2026-2920
Preprint. Discussion started: 12 June 2026

2.2 Model configuration

C-Star uses ROMS-Tools (Loose 2026) for the generation of grid and input files, and executes an updated version of the Regional Ocean Modeling System (ROMS; Shchepetkin and McWilliams 2005), coupled to the Marine Biogeochemical Library (MARBL; Long et al. 2021). Our model is configured with four nests, spanning 2.5 km resolution in the outer domain to 50 m in the inner-most nested domain (Figure 2). The outer nest uses data from the Global Ocean Physics Reanalysis dataset (GLORYS 12v1) for lateral boundary and initial conditions (Jean-Michel et al. 2021), while the inner nests use lateral boundary and initial conditions from their respective parent domains. All nests are forced with the fifth generation ECMWF global reanalysis dataset (ERA5) for surface forcing (31 km grid spacing; 10 m wind velocities, short and longwave radiation, 2 m air temperature, total precipitation and absolute humidity; Hersbach et al. 2020) and the TPXO dataset for tidal forcing (Egbert and Erofeeva 2002). The two outermost nests use the SRTM v2.5 dataset for bathymetry (OpenTopography 2020), while the two innermost nests use EMODnet bathymetry (EMODnet Bathymetry Consortium 2022), which has higher spatial resolution but does not cover the entire domain for the two outer nests. The inner nests' bathymetry is smoothed along the boundaries to match the parent bathymetry. The two outermost nests have no river forcing, while the two innermost nests are forced with the Hvalfjörður river-dataset, which is based on a survey done on the 25th of July, 2024 (see Supplement and Fig. S1 for more details).

Lateral boundary conditions, surface forcing and initial conditions for biogeochemical constituents are derived from a combination of observational and model-based sources. Nitrate, phosphate, silicate and dissolved oxygen are obtained from the 2018 World Ocean Atlas (Zweng et al. 2019); dissolved iron is interpolated from a data-driven model dataset (Huang et al. 2022). Dissolved inorganic carbon (DIC) and alkalinity are from the global GLODAPv2 product (Olsen et al. 2016), and atmospheric CO_2 forcing is obtained from Landschützer et al. (2016) and dust is obtained from Kok et al. (2020). Other surface fields (iron, NOx and NHy), as well as ammonium and dissolved organic matter (for which there are no gridded observational projects available), are obtained from ocean biogeochemical simulations produced with the global Community Earth System Model (CESM) model simulation (Yeager et al. 2022).

https://doi.org/10.5194/egusphere-2026-2920
Preprint. Discussion started: 12 June 2026

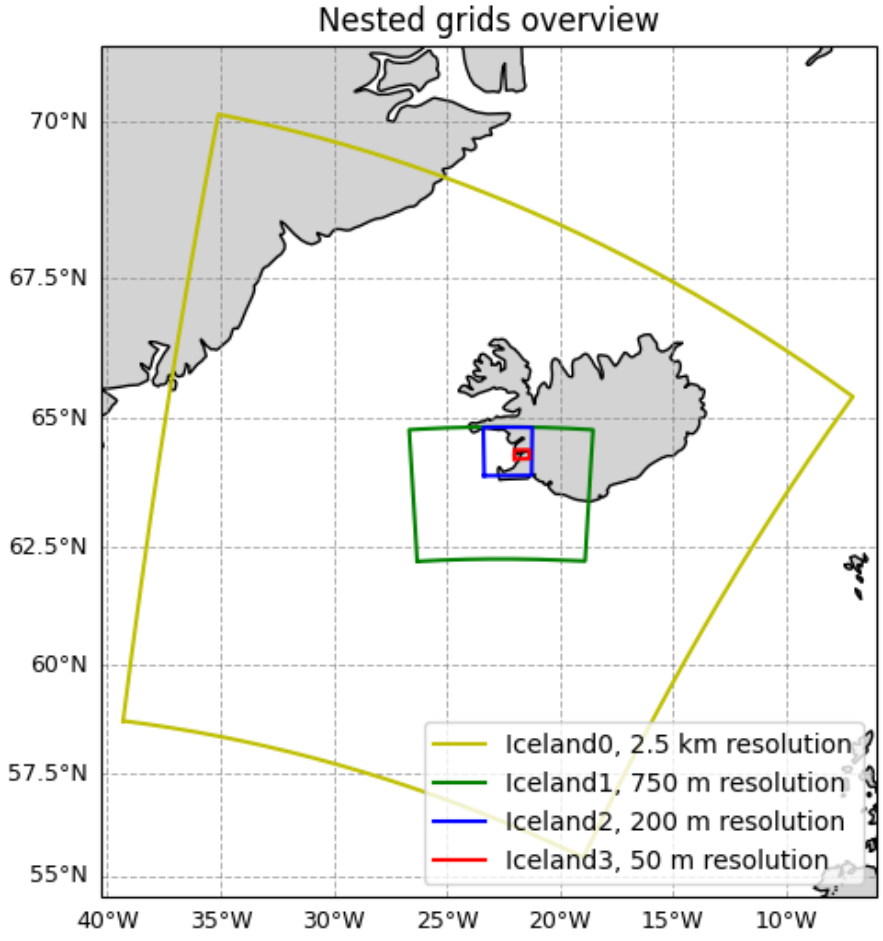

Figure 2. Overview of nested grids for the Hvalfjörður domain with the spatial extent and resolution for each grid.

The model simulations cover February through November 2024 for the three outermost nests, while the inner 50 m resolution nest is only run for the months of July and November due to computational costs. The setup scripts are available at (Heede 2026) : https://cworthy-ocean.github.io/C-Star-in-Hvalfjordur/

2.3 Observational data

Observational datasets used for model-observation comparison consist of CTD profiles (Harðardóttir et al. 2026a) and discrete samples (Harðardóttir et al. 2026b) collected on a series of 20 cruises conducted by the Iceland Marine and Freshwater Research Institute (MFRI) from April 2024 to April 2025, along with time series from moorings (Harðardóttir et al. 2026c) deployed at 5 locations across Hvalfjörður during the same period. Tidal gauge data is obtained from the meteorological station located at Grundartangi (Icelandic Meteorological Office).

https://doi.org/10.5194/egusphere-2026-2920
Preprint. Discussion started: 12 June 2026

For physical state variables (salinity and temperature) along with fluorescence and dissolved oxygen, a series of profiles was obtained with 1 m vertical resolution by conducting casts using a Sea-Bird SBE25 CTD, at up to 12 stations (Fig. 1). For some cruises, only a subset of CTD casts at the 12 stations were carried out due to weather and tidal conditions. Water samples were collected using a Seabird SBE55 water sampler at 4 to 7 of the 12 stations, at depth intervals of 10 m to 30 m. Total alkalinity (TA), dissolved inorganic carbon (DIC), pH, SiO_2, PO_4, NO_3, and chlorophyll were analyzed for each sample.

The five moorings were equipped with upward looking RDI Teledyne Workhorse Sentinel 300 kHz ADCPs, measuring eastward (u) and northward (v) velocities at 4 m depth intervals. Additionally, time series of temperature, salinity, pressure, and dissolved oxygen were obtained with Sea-Bird SBE37SMP-ODO MicroCATs, located at ca. 30 m depth. In the inner fjord next to station 10, additional pH time series were obtained from a Sea-Bird Deep SeapHOx located at 60 m depth. The mooring data cover the period from April 2024 to April 2025.

2.4 SF_6 release, underway data collection and passive tracer release simulations

To evaluate the model's fidelity in simulating tracer dispersion, we used data from a dual-tracer release experiment in Hvalfjörður, where a known ratio of helium-3 (^3He) and sulfur hexafluoride (SF_6) was injected into the surface mixed layer on 17 July 2024 along a transect from 64.3974 °N, 21.6455 °W to 64.3710 °N, 21.6128 °W (see Fig. 1b; Gerke et al., 2026). Following the release, the patch of tracer-infused seawater was tracked using an underway analytical system installed aboard a research vessel running multiple transects through the fjord daily. Full details of the tracer release, sampling strategy, and post-processing are provided by Gerke et al. (2026), and the instrumentation follows established approaches in Ho et al. (2002).

To match the SF_6 release as closely as possible in a model simulation, a dye tracer is released in the Iceland2 model domain (Fig. 2), in a line one grid cell wide (200 m), which tracked the observed line of SF_6 release at 1 p.m. on July 17th, 2024 local time (see Fig. 1b) and the model was then integrated forward for 10 days. The depth of the release was set to the model level corresponding to approximately 2 m, as this was the depth at which maximum concentrations were measured a few hours after the release (Gerke et al. 2026). The tracer concentration in our simulation was scaled to match the observed SF_6 concentrations measured in the hours following the release. We do this because released SF_6 only partially dissolves in the seawater, reaching an unknown saturation state during the bubbling process. As is standard, we then assume no subsequent air-sea SF_6 exchange over the following 10 days of the simulation.

https://doi.org/10.5194/egusphere-2026-2920
Preprint. Discussion started: 12 June 2026

2.5 OAE simulations

An ensemble of six OAE simulations was conducted representing the release of an alkalinity-enriched solution near a pier at the head of the fjord (see Fig. 1b). Three simulations were performed in November with no river runoff in the model (to reflect colder winter conditions with minimal river runoff (see supplementary section 1), and three in July with river runoff. The ensemble members additionally spanned different tidal and wind conditions, with the goal of capturing a wide range of physical transport and mixing responses, as illustrated by Fig. S2 and summarized in Table 1.

Each of the 6 ensemble members simulated the discharge of a 4.5% NaOH solution (1.18×10^6 mmol m^{-3}) and a flow rate of 30 L min^{-1} over a 96-hour period (204 kmol alkalinity released in total). The addition of alkalinity and freshwater was specified as a volume flux within a single grid cell over the specified duration, and the salinity of the release volume was set to 1 psu (nominal value representative of freshwater) and the temperature to 10°C, while all other tracers were set to zero. These values were selected to approximate a realistic, small-scale field trial involving the discharge of a NaOH solution diluted with freshwater, while remaining within operational and environmental safety constraints. The configuration was designed to produce a detectable, short-lived signal in alkalinity, pH, and pCO_2 in the vicinity of the release site without inducing large or long-term alterations to the fjord's biochemistry. These alkalinity release simulations were implemented via a specialized forcing module within C-Star.

The simulation leverages the two parallel carbonate systems implemented in MARBL, which are subject to identical physical transport and biogeochemical source–sink processes. By applying the alkalinity perturbation exclusively to one tracer system, the model effectively isolates the impact of the OAE intervention, allowing direct comparison against an internally consistent baseline that evolves under identical circulation and mixing.

https://doi.org/10.5194/egusphere-2026-2920
Preprint. Discussion started: 12 June 2026

	Tidal range (min and max)	Average wind speed	Typical wind direction (mode)	Avg. surface temperature and salinity	Avg. bottom temperature and salinity	Water column stratification
CDR1 (July 12th)	1.11 m - 2.64 m	4.7 m/s	175°	12.0°C 33.4 psu	11.6°C 34.4 psu	0.879 kg/m^3
CDR2 (July 14th)	1.11 m - 3.35 m	3.5 m/s	165°	12.0°C 33.4 psu	11.6°C 34.4 psu	0.879 kg/m^3
CDR3 (July 16th)	1.26 m - 3.80 m	3.9 m/s	325°	12.0°C 33.4 psu	11.6°C 34.4 psu	0.879 kg/m^3
CDR4 (November 5th)	1.48 m - 3.09 m	9.1 m/s	125°	5.4°C 33.7 psu	5.6°C 33.9 psu	0.166 kg/m^3
CDR5 (November 9th)	1.48 m - 3.89 m	9.5 m/s	245°	5.4°C 33.7 psu	5.6°C 33.9 psu	0.166 kg/m^3
CDR6 (November 17th)	2.32 m - 4.01 m	7.4 m/s	15°	5.4°C 33.7 psu	5.6°C 33.9 psu	0.166 kg/m^3

Table 1. Overview of the modeled tidal, wind and seasonal conditions for the OAE simulations.

We used data from the MFRI field campaign described in Section 2.3, along with a timeseries of pCO_2 data from a sensor installed by Röst Marine Research Centre to estimate levels of background variability based on the standard deviation of surface pCO_2, alkalinity, pH and DIC. These data are used to estimate levels of detectability of signals in the carbonate chemistry system stemming from the OAE experiments as described in more detail in the caption for Table S2.

In addition to the simulations with physical circulation and MARBL biogeochemistry, we constructed two simplified carbonate chemistry scenarios using CO2SYS (Lewis et al. 1998) to isolate the role of background conditions in determining the response to alkalinity addition. In these experiments, alkalinity was added in the same manner as in the fully coupled simulations, but carbonate system changes were calculated diagnostically under steady background conditions without air–sea interactions. Two background states were considered: one based on modeled background alkalinity, DIC, nutrients, temperature, and salinity, and one based on observed background conditions (Table S1). In order to isolate the effects of biases in surface alkalinity, DIC, temperature and salinity on the model's ability to accurately simulate pCO_2 anomalies created in response to the OAE intervention, we considered pCO_2 as a function of DIC, alkalinity, temperature and salinity:

$$f = f(DIC, ALK, T, S) \quad (1)$$

https://doi.org/10.5194/egusphere-2026-2920
Preprint. Discussion started: 12 June 2026

Where f represents pCO_2 as calculated using CO2SYS. The change in pCO_2, δf, resulting from the alkalinity intervention I is:

$$\delta f = f(DIC, ALK + I, T, S) - f(DIC, ALK, T, S) \quad (2)$$

We approximate f using the sensitivity of pCO_2 to alkalinity, Θ:

$$\delta f \approx \Theta \cdot I \quad (3)$$

$$\Theta = \frac{dpCO_2}{dAlk} \quad (4)$$

To estimate the contribution of biases in all four state variables (*DIC, Alk, T, S*) to the simulated change in pCO_2 owing to alkalinity addition we calculated the sensitivity of to *DIC, Alk, T* and *S* and multiplied each sensitivity with the respective bias, and then multiplied the sum of the bias terms with the intervention, *I*:

$$\Delta(\delta f) = \left(\frac{\partial \Theta}{\partial DIC}\Delta DIC + \frac{\partial \Theta}{\partial Alk}\Delta Alk + \frac{\partial \Theta}{\partial T}\Delta T + \frac{\partial \Theta}{\partial S}\Delta S\right) \cdot I \quad (5)$$

Where $\frac{\partial \Theta}{\partial X}$ is evaluated at the observed state, and *X* represents four different carbonate system variables (*DIC*, *Alk*, *T* and *S*) (Middelburg et al. 2020).

In addition, we define max as the maximum theoretical uptake of CO_2 per added alkalinity once the system has fully equilibrated (i.e. pCO_2 has returned to its pre-intervention value, Zhou et al. 2025):

$$\eta_{max} = \left(\frac{\delta DIC}{I}\right)_{pCO_2} \quad (6)$$

Where δDIC represent the total perturbation to DIC as a result of the intervention, *I*. Next, we estimate the sensitivity of η_{max} to the model biases using a similar approach as above:

$$\Delta\eta_{max} = \frac{\partial \eta_{max}}{\partial DIC}\Delta DIC + \frac{\partial \eta_{max}}{\partial Alk}\Delta Alk + \frac{\partial \eta_{max}}{\partial T}\Delta T + \frac{\partial \eta_{max}}{\partial S}\Delta S \quad (7)$$

Here we neglect the impact of the intervention itself as it is negligible for small alkalinity additions (Yankovsky et al. 2025).

https://doi.org/10.5194/egusphere-2026-2920
Preprint. Discussion started: 12 June 2026

3 Results

3.1 Model Evaluation

3.1.1 Circulation

The model solution for the 50 m resolution domain shows a classic fjord circulation pattern with outflow in the upper 5 m and inflow below 10 m, peaking at 20 m depth. Superimposed on this pattern, the model also reveals a counter-clockwise circulation with the outflow strongest along the northern coastline and the inflow strongest along the southern coastline (Fig. 3).

Hvalfjörður exhibits a strong tidal flow that is well-represented by the model. Sea-surface height variations closely match tidal gauge observations (Fig. 4), and spectral analysis of velocity data shows a strong diurnal peak consistent with the model (Fig. S3). In addition, the magnitude, direction and temporal variability of velocity from the ADCP moorings are overall consistent with the model (Figs. 5 and Fig. S4).

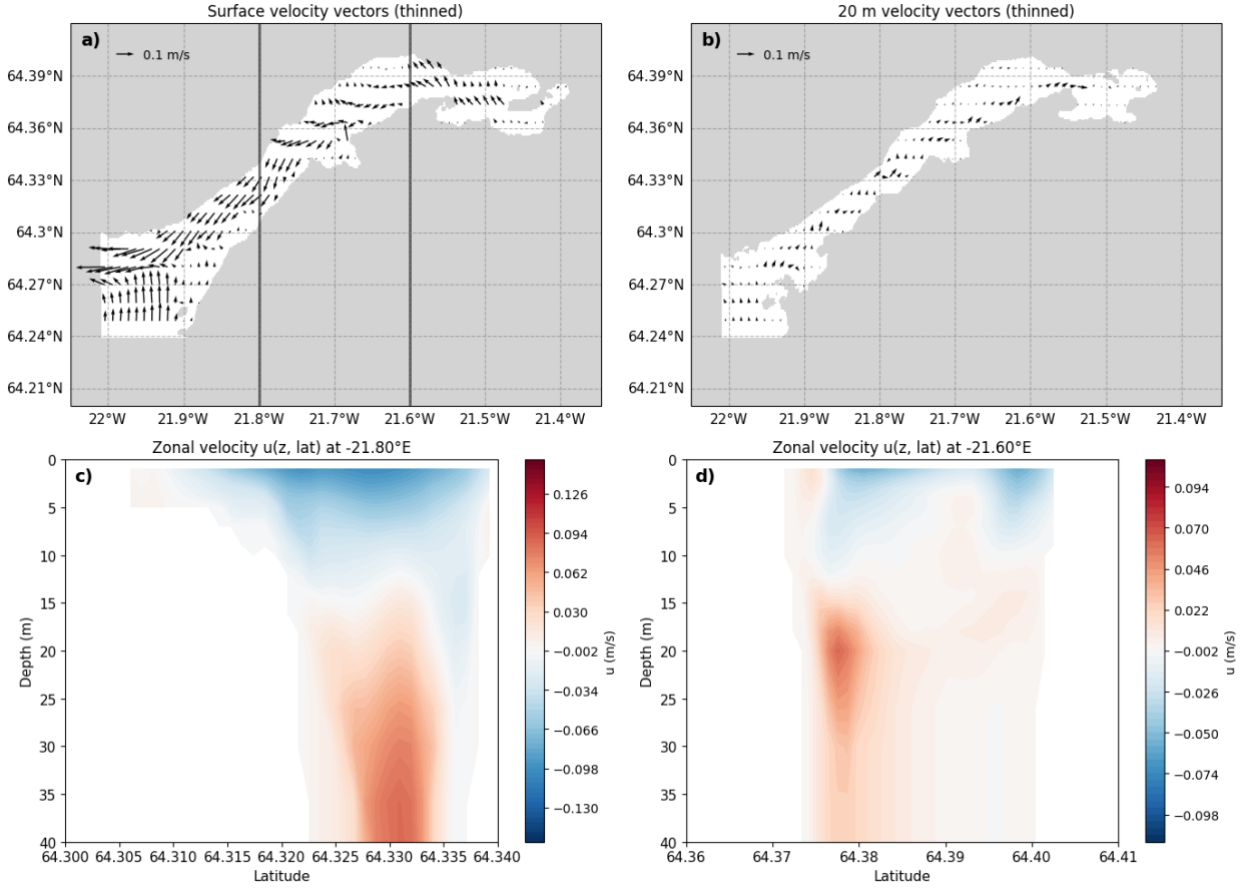

https://doi.org/10.5194/egusphere-2026-2920
Preprint. Discussion started: 12 June 2026

Figure 3. Time averaged simulated lateral flow at a) the surface, b) and at 20 m depth from July 2024 in the Iceland3 (dx = 50 m) domain (the vectors have been subsampled so every 10th vector is shown). South-North cross-sections of eastward velocity across c) the outer fjord at 21.8 °W and d) the inner fjord at 21.6 °W.

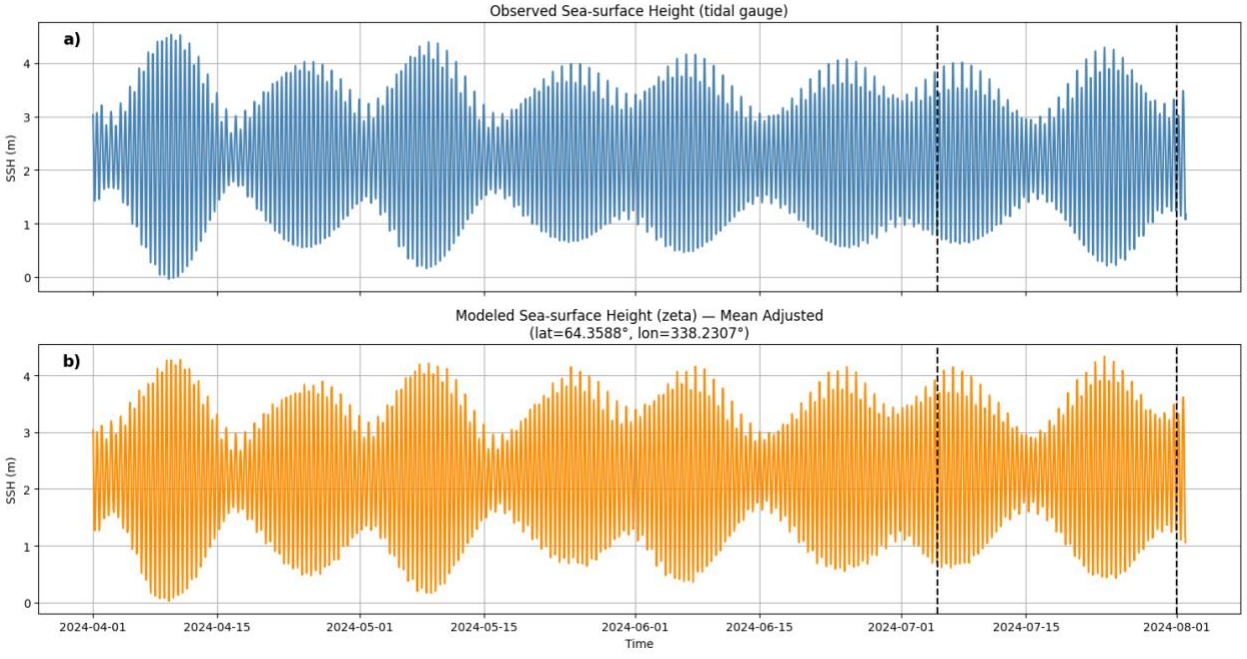

Figure 4. Sea-surface height (SSH) comparison between a) a tidal gauge located at Grundartangi (see location in Fig. 1) and b) SSH from model output covering the period April, 2024 to August 2024 for the Iceland2 domain (dx=200 m). The dotted lines indicate the period shown in Fig. 5. Note that the modeled SSH values have been adjusted to have the same mean value as the tidal gauge.

https://doi.org/10.5194/egusphere-2026-2920
Preprint. Discussion started: 12 June 2026

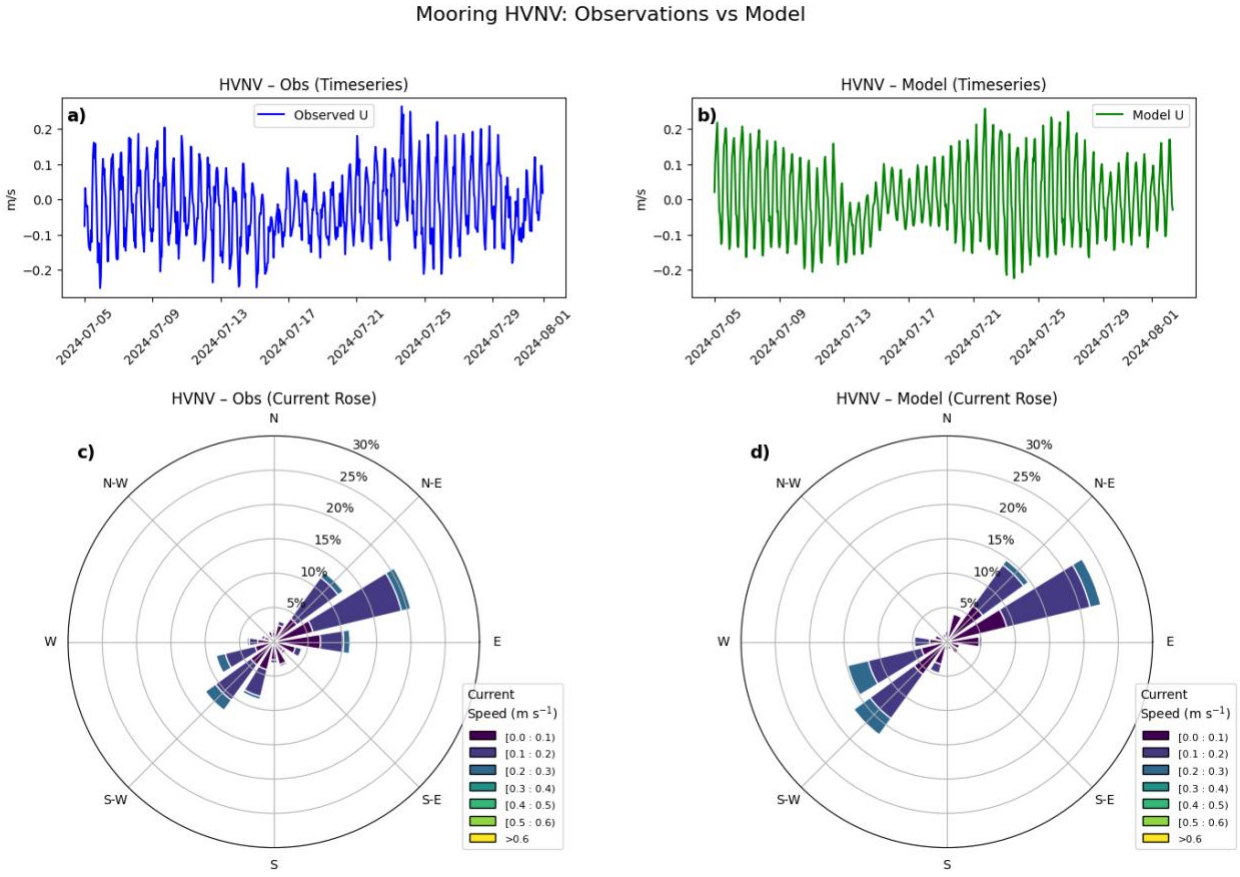

Figure 5. Model–observation comparison of velocity at mooring HVNV. Ten-minute averages of a) observed and b) simulated eastward velocity at 10 m depth are shown for the period 5–31 July 2024 for the Iceland2 domain (dx=200 m). c–d) Current rose diagrams derived from the same time series illustrate the distribution of current direction and speed for the observed and simulated velocities, respectively. In the current rose, the angular position indicates the direction toward which the current originates, while the radial extent represents the percentage of occurrence (frequency) of currents from that direction. Colored segments denote current speed bins (m s⁻¹), with longer sectors indicating more frequent currents in that direction and speed range.

3.1.2 Salinity and temperature

Fig. 6 compares time-averaged salinity fields from April to September 2024 between observations and the model, shown as along-fjord and across-fjord sections. Overall, the simulated salinity distribution reproduces the principal structures evident in the observations, including the upper ocean halocline and the horizontal gradient from the inner to the outer fjord. However, in the innermost fjord, the model is approximately 1.5 psu fresher than observed; conversely, in the outer fjord at depth, the model is about 0.5 psu too salty relative to observations. These discrepancies point to a salinity bias in the boundary conditions, along with possibly excessive inner-fjord freshwater forcing, or that the simulated estuarine circulation in the fjord is too weak. Sensitivity tests indicated that the estuarine circulation is sensitive to changes in the bottom drag

https://doi.org/10.5194/egusphere-2026-2920
Preprint. Discussion started: 12 June 2026

parameterization, with reductions in the specified drag coefficient producing simulations with enhanced overturning. Furthermore, stratification and overturning biases are likely sensitive to the vertical mixing parameterizations.

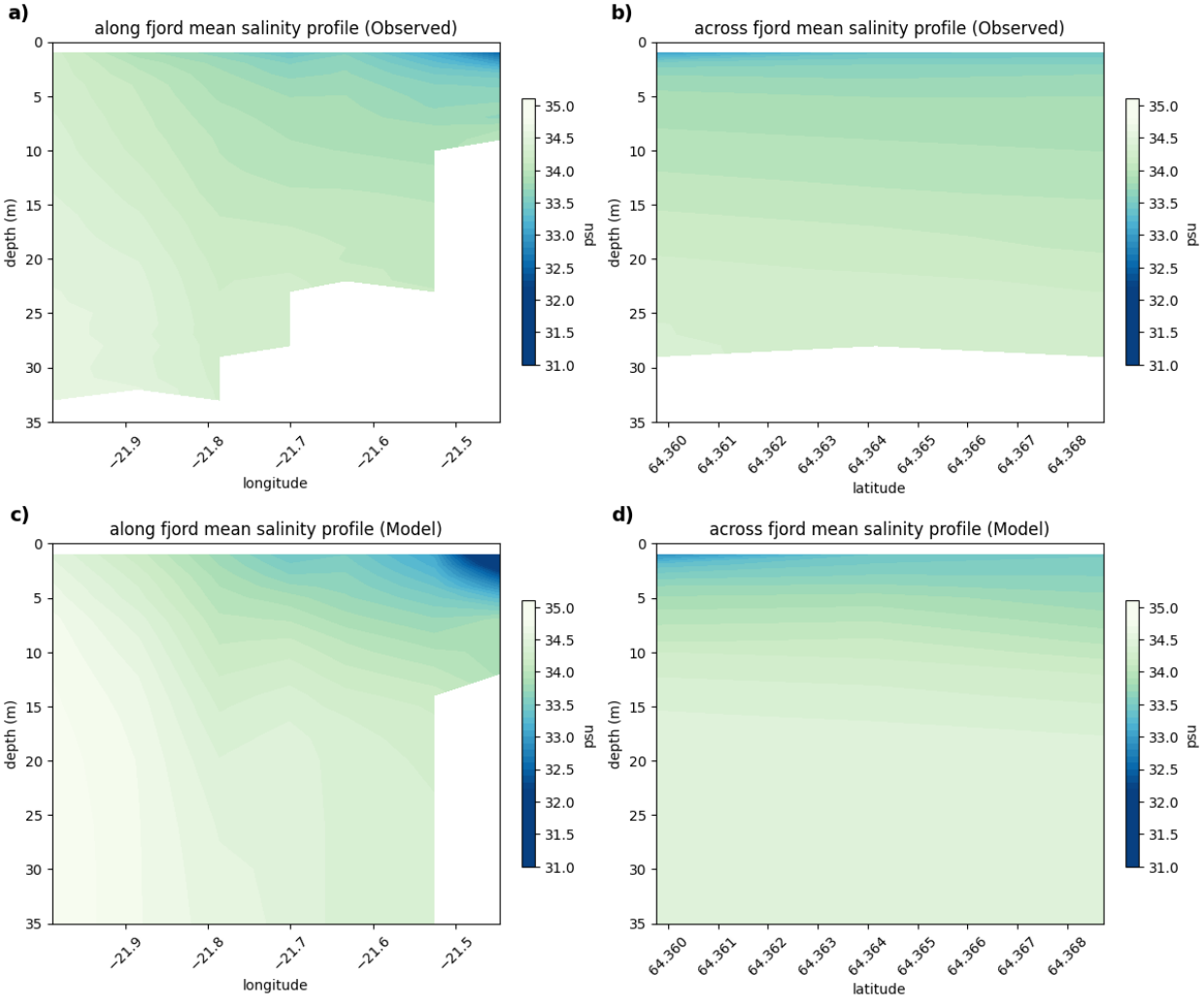

Figure 6. Time-averaged salinity from April 2024 to September 2024 shown as a) an along fjord profile calculated from CTD stations 1, 3, 5, 7, 9 and 10 and b) a fjord cross-section calculated from CTD stations 6, 7 and 8. c) and d) are the modeled salinity values from the corresponding locations averaged over the same timeframe.

In terms of the seasonal evolution of stratification, the model captures the freshening of surface waters in spring, indicating that the timing of the freshwater input is reasonably represented. However, the additional surface freshening observed in November is not reproduced, suggesting that the freshwater forcing was 'shut off' too early (Fig. 7a). Temperature-driven stratification remains weak throughout the water column, consistent with observations, but the fjord undergoes rapid seasonal warming from approximately 2.5°C in April to about 11°C in August (Fig. 7b). The model reproduces the timing

https://doi.org/10.5194/egusphere-2026-2920
Preprint. Discussion started: 12 June 2026

and general structure of this warming — but overshoots, reaching a positive temperature bias of roughly 1°C in August. This warm bias is likely a result of excessive shortwave radiative forcing or biases in the surface heat fluxes, implying that the provided atmospheric forcing may be too warm, too humid, or insufficiently windy, which would reduce evaporative cooling in the bulk flux parameterizations.

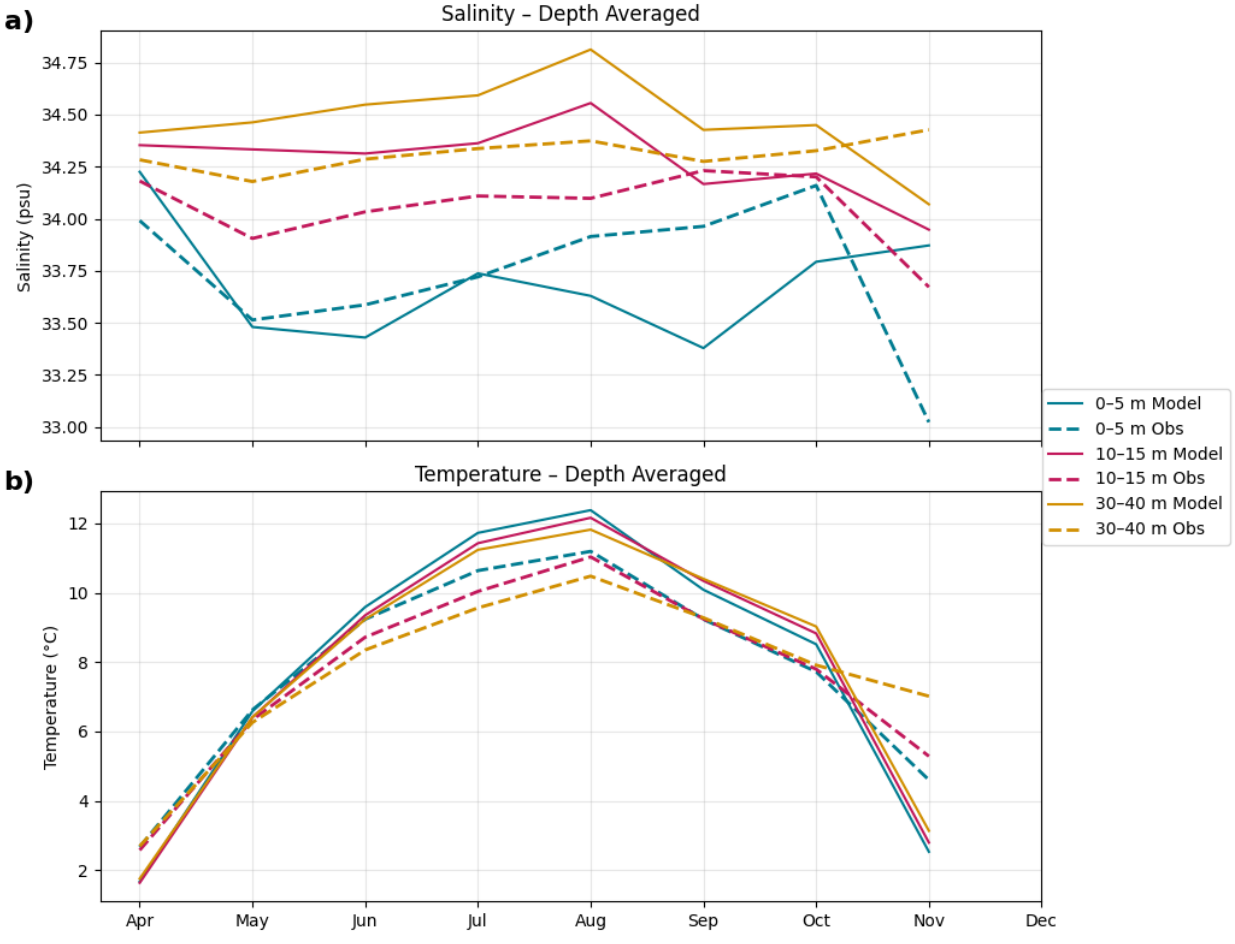

Figure 7. Seasonal evolution of a) salinity and b) temperature in the fjord averaged across 10 CTD stations for three different depth intervals. Dashed lines: observations; solid lines: model values from the corresponding CTD station locations.

3.1.3 Tracer dispersal

The comparison between ship-based underway SF_6 measurements and the modeled dye tracer release reveals alignment in the scales of surface dispersal and transport dynamics. Following the initial injection at approximately 21.63 °W, the observed tracer concentration exhibits a two orders of magnitude decrease in peak values within the first four days, a period

https://doi.org/10.5194/egusphere-2026-2920
Preprint. Discussion started: 12 June 2026

during which the median longitudinal location of the material is transported toward the mouth of the fjord. The tracer on day 1 is highly concentrated near the release, and on day 2 shows a bi-modal distribution. On day 3 and onwards, the tracer is evenly distributed throughout the fjord (Fig. 8a).

The modeled tracer release shows a similar reduction in tracer magnitude over the four-day window and a similar median tracer position. The model likewise shows the tracer highly concentrated on day 1, bi-modally distributed on day 2 and evenly distributed on day 3, though the peak concentration locations are slightly different. Some sampling bias may exist in the observational record due to limited coverage on specific days, as the spatial distribution of these ship-based samples varies by day (Fig. S5 and Fig. S6). Despite those constraints, the overall agreement between model and observations suggests that the model accurately captures the bulk characteristics of surface-layer dispersal and transport within the fjord (Fig. 8b).

https://doi.org/10.5194/egusphere-2026-2920
Preprint. Discussion started: 12 June 2026

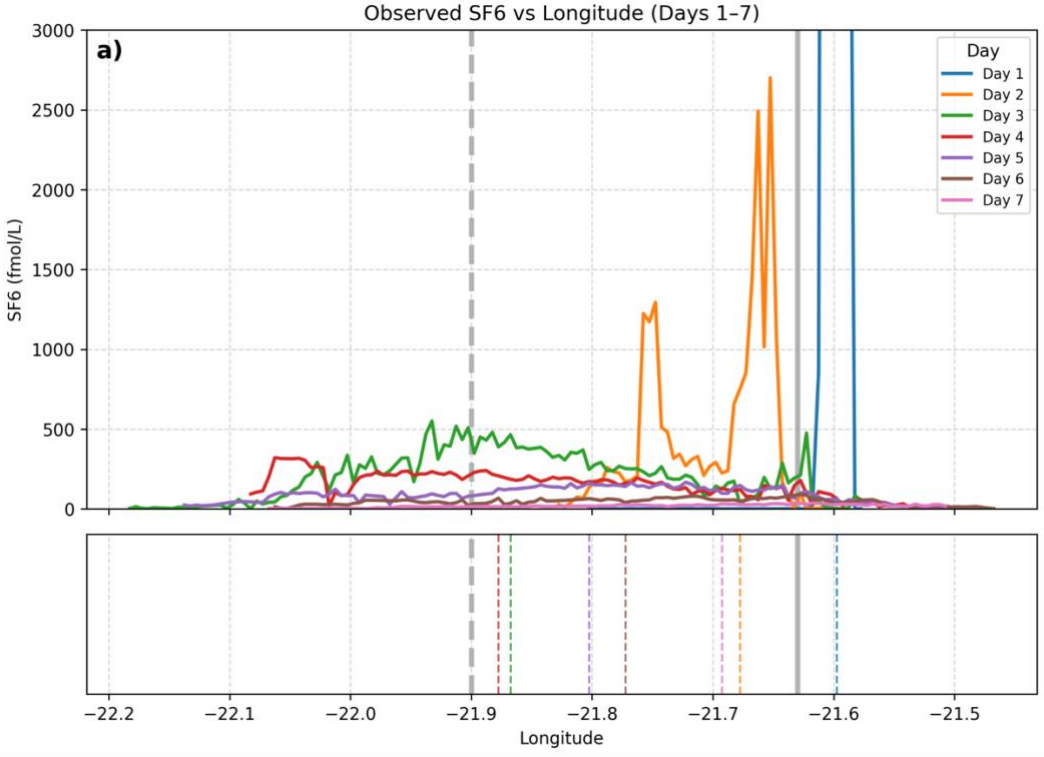

335

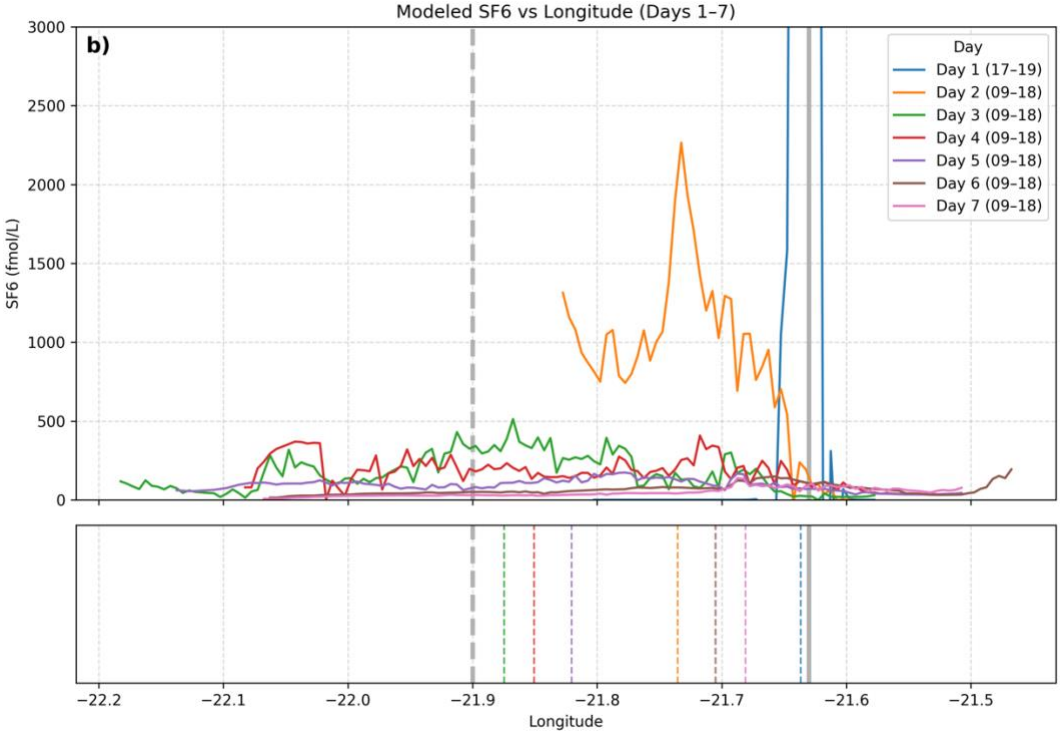

https://doi.org/10.5194/egusphere-2026-2920
Preprint. Discussion started: 12 June 2026

Figure 8. Daily averaged tracer concentration as a function of longitude for a) the observed underway SF_6 measurements (Fig. S4) and b) the modeled tracer sampled at the locations and times where observations are taken each day. The data are binned in 0.02 degree longitude bins. The boxes below the main plot show the median longitudinal location of tracer concentration for each day (based only on the sample locations from that day). Note that the model tracer concentration is scaled with a single value for all days to match the binned peak concentration on Day 1 (see Fig. S7). The grey line indicates the injection longitude, and the stippled grey line indicates the mouth of the fjord.

3.1.4 Alkalinity and DIC

Both alkalinity and DIC in the model solution exhibit a persistent negative bias of about 60 mmol m-3 throughout the water column relative to observations (Fig 9b,d). Despite this offset, the model reproduces the overall vertical structure of total alkalinity and DIC, indicating that the large-scale profile shape and stratification (primarily a function of salinity) are realistically represented. However, when examining salinity-normalized alkalinity and DIC, a structural discrepancy becomes apparent: the model fails to reproduce the observed decline in surface DIC relative to depth (Fig 9c). The mean negative bias in both DIC and alkalinity likely reflects inaccurate biogeochemical boundary forcing derived from coarse-resolution global datasets that do not resolve near-coastal biogeochemical conditions. In addition, the absence of a clear surface-to-depth DIC gradient in the model suggests deficiencies in subsurface remineralization processes, which would influence vertical carbon redistribution.

https://doi.org/10.5194/egusphere-2026-2920
Preprint. Discussion started: 12 June 2026

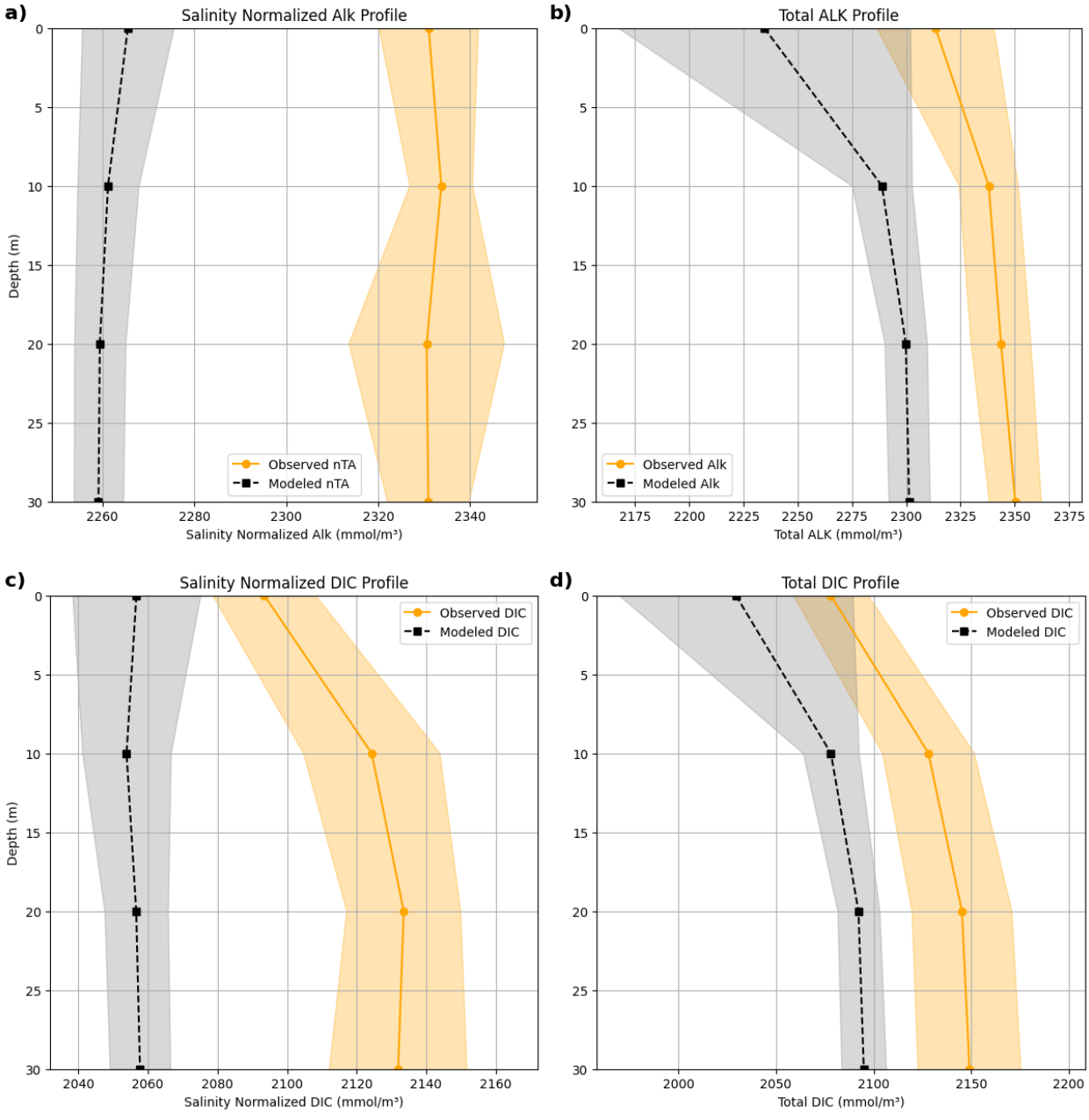

Figure 9. Time-averaged modeled and observed alkalinity and DIC profiles from April to September 2024. a) and c) plots show the salinity normalized profiles, and d) and e) show the total profiles. The orange shaded area represents one standard deviation of variation across measurements. The grey shaded area is the standard deviation of model data sampled at observed locations and days.

A supplementary analysis of nutrients and dissolved oxygen (Fig. S8 – Fig. S10) supports the interpretation of insufficient remineralization at depth in the model, likely driven by reduced biologic productivity overall. Both observations and simulations show a decline in nutrients during April, consistent with a spring bloom, but in the model, the nutrient drawdown

https://doi.org/10.5194/egusphere-2026-2920
Preprint. Discussion started: 12 June 2026

is much more muted, and chlorophyll concentrations are lower. We suspect that diatoms and small phytoplankton in the model are iron-limited (Fig. S9), but additional research is needed to confirm this. In addition, the model has excessive O_2 saturation relative to observations (Fig. S10), further supporting the inference that the model underestimates respiratory oxygen consumption at depth.

3.2 Simulation of OAE field trials

3.2.1 Simulated signal detectability

Fig. 10 illustrates that the added alkalinity from the ensemble mean of the July OAE experiments generates a detectable signal (as defined by 1 to 2 standard deviation of background variability defined in Table S2 and described Section 2) confined to a 1 km^2 area around the release location. This spatial footprint is evident in a depression in surface ocean pCO_2 (Fig. 10a), elevated pH (Fig. 10b), and increased alkalinity (Fig. 10c) in the vicinity of the discharge site. The corresponding time series (Fig. 10e–g) demonstrate that the maximum surface anomalies fluctuate in phase with tidal currents rather than accumulating monotonically over the course of the release, as the tidal flow alternately concentrates and disperses the alkalinity-enriched water. Once the release ceases, the alkalinity and pH signals return to baseline conditions within approximately 12 hours (24 hours for surface pCO_2). Although instantaneous peak pH values approach 9.3 (Fig. 10f), the spatially averaged pH within the affected zone remains substantially lower, around 8.2 (with a background value of around 8.1) throughout the experiment, indicating that any large pH excursions will be highly localized and transient. In the November experiments, the detectable signal area is much smaller (100 m), likely due to stronger surface winds and less water-column stratification, which subjects the area near the release to strong vertical mixing and dispersion (Fig. S11).

Modeling results suggest that surface wind conditions strongly influence the magnitude of the OAE signal. Maximum pH excursions and minimum surface pCO_2 generally occur during periods of relatively calm winds, such as the beginning of the CDR3 release and the latter half of the CDR2 release, when alkalinity-enriched surface waters remain more concentrated near the discharge site. In contrast, CDR1 takes place under persistently windy conditions and exhibits smaller maximum pH excursions, indicating that surface winds play an important role in the lateral dispersal of the alkalinity signal (Fig 3f). In the November simulations, which have average wind speeds 5 m/s stronger than the July experiments, peak concentrations of alkalinity are about half the magnitude of those in the July simulations (Fig S3g), with CDR5 experiencing higher peak concentrations than CDR4 and CDR6, corresponding to brief lulls in the winds around 30 hours after the release.

DIC anomalies are highest near the release point in all July simulations (Fig. 10d), but the maximum modeled DIC anomaly remains below the natural DIC fluctuations in the fjord at approximately 0.8 mmol m^{-3} in both July and November experiments (Fig. 10h, Fig. S12h). This reflects the fact that, although the total DIC anomalies will approach the alkalinity anomalies over time (see description of η_{max} in the methods section), this signal develops more gradually and is dispersed over a larger volume than can be captured over the simulated 8 days. As a result, while pH and alkalinity anomalies are pronounced and readily detectable in the near field of the release, the corresponding DIC signal is more spatially diffuse and

https://doi.org/10.5194/egusphere-2026-2920
Preprint. Discussion started: 12 June 2026

temporally distributed, making it comparatively subtle. As a result, direct detection of enhanced carbon removal based solely on DIC measurements would be challenging under realistic observational constraints (Table S2).

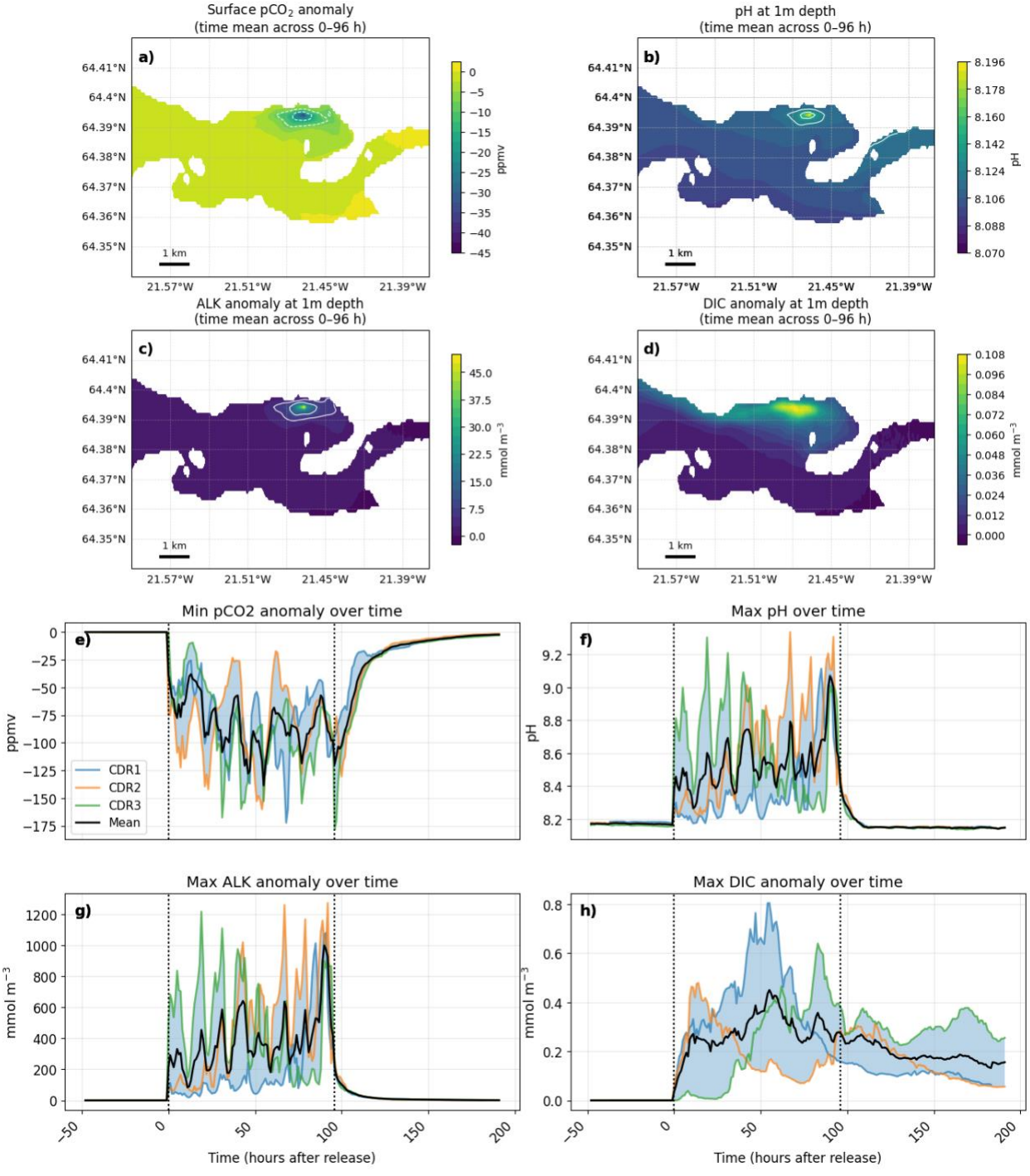

https://doi.org/10.5194/egusphere-2026-2920
Preprint. Discussion started: 12 June 2026

Figure 10. July response of the carbonate system to 96-hour point-source alkalinity releases. Panels (a–d) show horizontal maps of anomalies in (a) pCO_2, (c) alkalinity, and (d) dissolved inorganic carbon (DIC), and absolute values of (b) pH averaged across the 96 hour release period and across three July ensemble members. Anomalies are calculated by subtracting baseline values from the corresponding fields in MARBL's secondary carbonate system. The two white contour levels represent anomaly concentrations equal to one and two standard deviations from the background variability (defined in Table S2). Time series of the (e) minimum surface pCO_2 and (f–h) maximum pH, alkalinity, and DIC anomalies (full depth). Shaded regions in panels (e–h) indicate the ensemble spread. Vertical dotted lines indicate the start and end of the alkalinity release period.

3.2.2 CO_2-uptake

Figure 11e indicates that 0.05 to 0.15 moles of CO_2 are absorbed from the atmosphere per mole of added alkalinity during the four days of release and the subsequent four days. The average uptake rate in the November experiments is twice as high as the July experiments, likely due to both stronger surface winds and colder surface waters, both facilitating more rapid air-sea gas exchange. The uptake range reflects uptake over a finite time window and within a bounded model domain; some material is advected out of the regional domain (Fig S11) and is therefore not accounted for in the integrated fluxes. In the real system, exported alkalinity would continue to drive CO_2 uptake beyond the fjord, but here we explicitly restrict the analysis to short-term, near-field uptake following the release. As such, these results should not be interpreted as differences in ultimate uptake efficiency across the ensemble.

Spatially, Figure 11a shows that the CO_2 flux within the 8-day simulation is highest in the immediate vicinity of the release site, consistent with the localized surface pCO_2 reduction, but the resulting DIC anomalies are progressively advected and dispersed throughout the fjord (Fig. 11b). It is clear that surface winds are a key driver of both CO_2 uptake and dispersal of alkalinity. For CDR1, which takes place during moderately windy conditions, the initial CO_2 uptake is fast, but the uptake curve plateaus as southerly winds push the material along the northern shore and out of the domain, such that 30% of the material has left the domain four days after the release ends (Fig. S11). For CDR3, the initial CO_2 uptake is slow due to calm conditions, but when winds do pick up after the release ends, the direction is northerly, and material is pushed further into the fjord, allowing the total domain-integrated uptake to exceed that of CDR1 because virtually all the alkalinity remains within the domain over the analysis period. In the November experiments, the strongest uptake happens in CDR4 and CDR5 experiments, which experience the overall strongest winds (>10 m/s). In contrast to the July experiments, all added alkalinity remains in the domain in the 8 days following the release start in the November experiments, and the fraction of material in the surface layer is much smaller (5%) than in the July experiments (up to 25%). This indicates that the added alkalinity is mixed into deeper water in the November experiments, likely due to both stronger winds and weaker stratification. Redistribution into deeper layers increases its residence time within the fjord, since outflow is concentrated in the upper ~5 m (Fig. 3). At the same time, the reduced stratification allows vertical exchange to remain sufficiently active for CO_2 uptake to proceed, even as alkalinity is retained below the surface.

https://doi.org/10.5194/egusphere-2026-2920
Preprint. Discussion started: 12 June 2026

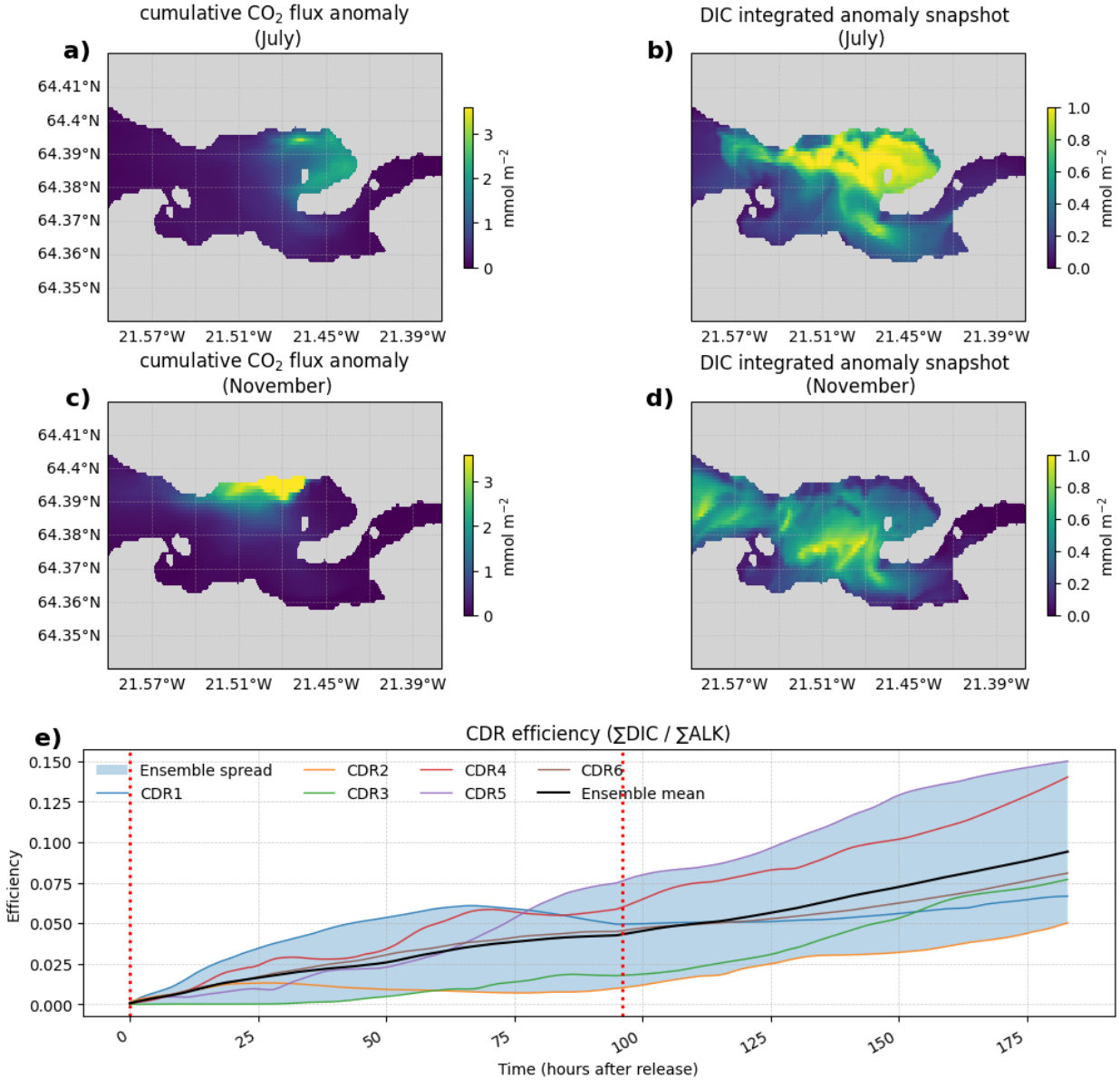

Figure 11. CO_2 uptake in response to the alkalinity enhancement experiment. a) Spatial distribution of the time-integrated CO_2 flux anomaly averaged across July ensembles (CDR1-3), b) depth-integrated ensemble averaged DIC anomaly at the end of the simulation, representing the total additional carbon stored within the water column 8 days after the release, averaged across July ensembles (CDR1-3). c-d) same as a-b) but for November ensembles (CDR4-6). e) Time-series of the CO_2 uptake (defined as moles per additional DIC per moles of additional alkalinity) where the red stippled vertical lines indicate the start and end of the alkalinity release period, and the shaded area indicates ensemble spread.

https://doi.org/10.5194/egusphere-2026-2920
Preprint. Discussion started: 12 June 2026

3.2.2 Sensitivity of OAE-generated-anomalies to biases in simulated background state

In order to assess the impact of biases in the model's simulated background state (described in section 3.1.4*)* on the magnitude of simulated anomalies, we first compare the maximum pH excursions simulated by the fully dynamic model with excursions estimated offline under the assumption of a static background carbonate system with the same amount of added alkalinity as in the full-model experiment (see methods). Two static background carbonate system scenarios were included, with average alkalinity, DIC, NO_3, PO_4, SiO_3, salinity and temperature fields taken from the observations and model during July (Table S1). The comparison in Fig. 12 indicates that biases in the model's background carbonate state do not significantly impair its ability to accurately simulate the system's response to the alkalinity perturbation. Instead, variability in pH is primarily driven by wind and tidally forced advection and mixing. This indicates that the modeled background carbonate system biases are not a first-order source of error in estimating peak pH excursions or their associated ecological impacts within the fjord domain. This further suggests that the initial pH response to alkalinity addition can be approximated by superimposing the alkalinity perturbation onto the background state, implying that a conservative tracer representation of alkalinity may be sufficient to estimate pH changes without requiring a fully coupled biogeochemical model.

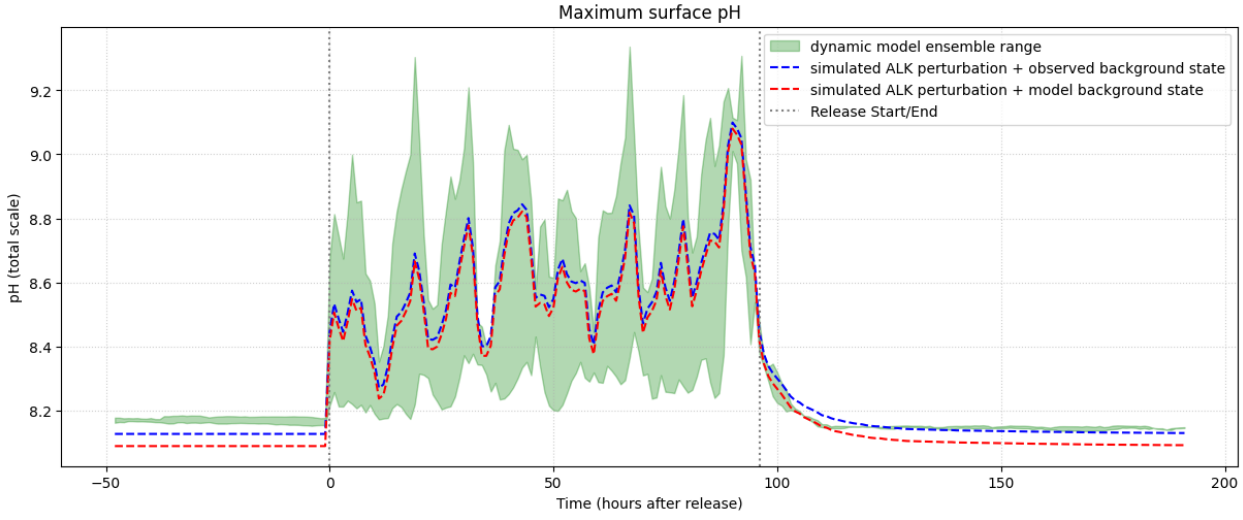

Figure 12. Time series of pH maximum perturbations in response to alkalinity release under three different background carbonate chemistry configurations. The green shaded area indicates the ensemble range of maximum pH excursions across the July ensemble members using the fully coupled dynamic model. The two additional scenarios assume constant background carbonate system conditions and compute pH excursions diagnostically using the alkalinity perturbation prescribed in the fully coupled model: (red) background alkalinity and DIC fixed to values derived from the model simulation, and (blue) background alkalinity and DIC fixed to observationally derived values.

Likewise, we can estimate the error in the pCO_2 response near the release site by assuming an intervention value, *I*, of +30 mmol/m^3 (the average value near the pier during the July release, see Fig. 10c) and calculate the resultant terms in equation (5) shown in Table 2. The results indicate that the background biases in DIC and alkalinity are mostly compensatory, yet the

https://doi.org/10.5194/egusphere-2026-2920
Preprint. Discussion started: 12 June 2026

temperature bias introduces an additional error of 3 µatm in the modeled pCO_2 anomaly, yielding a total negative (over-estimation) bias of 5 µatm, which is around 10% of the average pCO_2 anomaly near the release site. Model biases change the theoretical maximum uptake, $\eta_{max,}$ only very minimally — by around 0.25% — increasing the maximum uptake efficiency from 0.858 to 0.860. This change again results from compensating biases in DIC and Alk, while the effects of temperature and salinity are negligible.

	Sensitivity ($\partial\theta/\partial X$)	Bias (X)	pCO_2 anomaly error	η_{max} error
DIC	-0.0124	-60.0 mmol/m³	-20.7 µatm	0.026
Alk	0.0115	-50.0 mmol/m³	18.7µatm	-0.024
T	-0.0651	1.5 T	-2.9 µatm	0.000
S	-0.0356	0.0 psu	-0.0 µatm	0.000
Total (sum of terms)			-4.9 µatm	0.003

Table 2. Attribution of pCO_2 and η_{max} anomaly biases. This table quantifies the sensitivity of the alkalinity-driven pCO_2 and η_{max} response to biases in the simulated background state in the model for July 2024. Sensitivities ($\partial\theta/\partial X$) are evaluated at the observed state using a central difference approximation. The pCO_2 and η_{max} anomaly errors for each variable represents the individual contribution of that parameter's bias to the total error in predicted pCO_2 or η_{max} change. A negative error indicates that the bias in that variable causes the model to overestimate the magnitude of the pCO_2 or η_{max} anomaly.

4 Discussion

Our main research goal is to document how a nested configuration of ROMS-MARBL setup using C-Star could be deployed to simulate perturbations and air–sea CO_2 fluxes owing to alkalinity addition in Hvalfjörður, Iceland. Our simulation of an ensemble of 96-hour releases in the inner fjord identified a localized area of approximately 1 km² with detectable anomalies in surface pCO_2, alkalinity, and pH in July experiments, and a much smaller (100 m²) area during November experiments. pH and alkalinity excursions did not increase monotonically throughout the experiments, but fluctuated in response to tidal flow and changing wind conditions, and returned to baseline levels within 12-24 hours after the release ended. We found that surface wind was a primary control on both horizontal dispersal and vertical mixing, regulating the dilution of added alkalinity and thereby modulating the resulting pH and pCO_2 responses. Under calmer conditions, reduced dispersal allowed alkalinity to remain concentrated near the release site, leading to larger pH excursions, while strong winds led to rapid mixing and dispersal of the added material. Hence, when planning a field trial aimed at achieving signal detectability, one might aim to conduct the experiment on days forecast to have light to moderate winds.

https://doi.org/10.5194/egusphere-2026-2920
Preprint. Discussion started: 12 June 2026

The uptake efficiency—defined as the moles of additional carbon absorbed from the atmosphere per mole of added alkalinity—ranged from 5–15% after 8 days from the start of the experiment, with peak uptake occurring within ~2 km of the release site. This efficiency is derived from the air–sea CO_2 flux and therefore reflects near-field uptake over the initial 8-day period, independent of whether the resulting DIC is later exported out of the domain. The peak DIC anomalies were low relative to background variability, indicating that confirming CO_2 uptake in the fjord via in situ DIC sampling would be difficult. Surface wind speed proved to be a key driver of CO_2 uptake in the domain, as strong winds led to rapid CO_2 uptake, particularly during the November experiments, when the water column was colder and more weakly stratified than in the July experiments. Note that in this study, we focused on the near-field detectability and carbon uptake. To determine the total CO_2-uptake from the experiments, a larger ocean domain would be necessary, or an application of an upscaling technique that passes the alkalinity and DIC values from a smaller domain to a larger domain.

To evaluate the framework's ability to simulate OAE experiments, we compared the simulation with observations collected during a 2024 field campaign, as well as with a tracer release and subsequent sampling. We confirmed that the model solution displayed a realistic counter-clockwise mean circulation with a strong tidal flow, and a comparison between observed and model tracer evolution showed that the model simulated realistic tracer dispersal and advection. The observed tidal currents, as well as sea-surface height variations from a tidal gauge, were well captured by the model solution. The fjord exhibited seasonal changes in temperature and salinity stratification, resulting in fresher, warmer waters throughout the summer months. This seasonal evolution was captured by the model solution, and could be refined by further constraining the time-varying volume of river input, and possibly tuning bottom roughness and vertical mixing parameters. Improved availability of river discharge data would provide critical constraints on freshwater forcing and reduce uncertainty in the modeled circulation and stratification.

Overall, these findings enhance confidence that a nested ROMS-MARBL model solution is well-posed for studying fjord-scale dispersal and advection of an alkalinity signal during and after an OAE release.

While the physical model solution captured key characteristics of the observed flow, we documented several biases in alkalinity, DIC, oxygen, nutrients and biologic activity. The model exhibited negative biases in background alkalinity and DIC, likely stemming from the coarse resolution of the global datasets used to initialize the biogeochemical model. In addition, the model had a positive bias in oxygen, oxygen saturation and nutrient concentrations. These discrepancies point to both biases inherited from initialization and boundary conditions, and specific local biological activity. Further evaluation and tuning would be required for MARBL to simulate these accurately, but this lies beyond the scope of the present study.

As we demonstrated using carbonate chemistry simulations under steady background conditions, alkalinity additions applied to the modeled background state produced pH and pCO_2 perturbations consistent with those obtained when evaluated

https://doi.org/10.5194/egusphere-2026-2920
Preprint. Discussion started: 12 June 2026

relative to the observed state, indicating that carbonate system nonlinearities did not significantly affect the simulated response in this case. Additionally, by conducting an ensemble of simulations, we found that circulation-driven variability, particularly from variations in surface wind conditions, appeared to be the dominant source of variability in estimating short-term pH excursions and near-field pCO_2 anomalies in this setting.

The model solution established here provides several avenues for future research in high-latitude estuary and coastal settings. Future model development work could focus on adapting parameters, forcing, and initialization datasets in MARBL to better reflect Hvalfjörður biogeochemical conditions, adding explicit benthic processes to the model, and incorporating future river gauge observations to further constrain freshwater influxes. In terms of model applications, this work has illustrated opportunities for explicitly deploying ROMS–MARBL nested model domains for OAE field-trial planning, anticipating maximum signal excursions, nearfield CO_2 uptake verification, and testing the sensitivity of OAE outcomes to variations in model parameters and configurations.

Code and data availability

All code used for model set-up, analysis and plotting is available here (Heede 2026): https://github.com/CWorthy-ocean/C-Star-in-Hvalfjordur. A description of how to obtain the datasets used to initialize the model, either by streaming or direct download, is available here: https://roms-tools.readthedocs.io/en/latest/datasets.html. Data from the 2024 MFRI field campaign are available here (Harðardóttir et al. 2026a, Harðardóttir et al. 2026b, Harðardóttir et al. 2026c): https://www.seanoe.org/data/01021/113246/ (moorings), https://www.seanoe.org/data/00993/110439/ (CTD) and https://www.seanoe.org/data/00992/110401/ (discrete samples). pCO2 sensor data may be obtained with permission from the Röst Marine Research Centre (contact Ulla Heede) and underway SF_6 data may be obtained from Lennart Gerke (lennart@cworthy.org). Model data cannot be hosted online (31 TB of data) but can be obtained from Ulla Heede by request (ulla@cworthy.org).

Author contributions

Ulla Heede led the conceptualization of the study and conducted the model simulations, and subsequent analysis, as well as developing methodology and software implementations, creating visualizations, and writing of the original draft and subsequent review and editing. Matt Long supervised U. H and contributed to conceptualization, methodology, software development (MARBL) and manuscript review and editing. He further was responsible for project administration and funding acquisition along with Alicia Karspeck who also contributed to manuscript review and editing. Scott Bachman contributed to methodology and software development (ROMS and C-Star). Nora Loose contributed to methodology, software (Roms-Tools), and manuscript review and editing. Dafydd Stephenson contributed to methodology and software

https://doi.org/10.5194/egusphere-2026-2920
Preprint. Discussion started: 12 June 2026

(ROMS, MARBL and C-Star). David T. Ho and Lennart Gerke contributed to data curation and provision of resources (SF6 field data) along with Tobias Koffman, and manuscript review and editing. Alice Benoit-Cattin contributed to data curation and provision of resources (MFRI observational data). Sara Harðardóttir contributed to data curation, provision of resources (MFRI observational data), and manuscript review and editing. Andreas Macrander contributed to data curation, provision of resources (MFRI observational data), validation, and manuscript review and editing.

Competing interests

The authors declare no competing interests.

Disclaimer

Copernicus Publications remains neutral with regard to jurisdictional claims made in the text, published maps, institutional affiliations, or any other geographical representation in this paper. While Copernicus Publications makes every effort to include appropriate place names, the final responsibility lies with the authors. Views expressed in the text are those of the authors and do not necessarily reflect the views of the publisher.

Acknowledgements

The authors are grateful for computational resources provided by the National Energy Research Scientific Computing Center (NERSC) and the National Science Foundation's Advanced Cyberinfrastructure Coordination Ecosystem (ACCESS).

Financial support

This research was funded by the Carbon to Sea Initiative.

References

Bashmakov, I. A., L. J. Nilsson, A. Acquaye, C. Bataille, J. M. Cullen, M. Fischedick, Y. Geng, and K. Tanaka, 2022: Climate change 2022: Mitigation of climate change. Contribution of working group III to the sixth assessment report of the intergovernmental panel on climate change, chapter 11.

Committee on A Research Strategy for Ocean-based Carbon Dioxide Removal and Sequestration, Ocean Studies Board, Division on Earth and Life Studies, and National Academies of Sciences, Engineering, and Medicine, 2022: A Research

https://doi.org/10.5194/egusphere-2026-2920
Preprint. Discussion started: 12 June 2026

Strategy for Ocean-based Carbon Dioxide Removal and Sequestration. National Academies Press, https://doi.org/10.17226/26278.

Egbert, G. D., and S. Y. Erofeeva, 2002: Efficient inverse modeling of barotropic ocean tides. Journal of Atmospheric and Oceanic technology, 19, 183–204.

EMODnet Bathymetry Consortium, 2022: EMODnet Digital Bathymetry (DTM 2022), https://doi.org/10.12770/ff3aff8a-cff1-44a3-a2c8-1910bf109f85.

Fennel, K., 2025: The Verification Challenge of Marine Carbon Dioxide Removal.

Friedlingstein, P., and Coauthors, 2026: Global Carbon Budget 2025. Earth System Science Data, 18, 3211–3288, https://doi.org/10.5194/essd-18-3211-2026.

Gerke, L., D. Ho, U. Heede, and T. Koffman, 2026: Limits on marine carbon dioxide removal potential set by coastal air-sea gas exchange rates, https://doi.org/10.21203/rs.3.rs-8745708/v1.

Gruber, N., and Coauthors, 2019: The oceanic sink for anthropogenic CO2 from 1994 to 2007. Science, 363, 1193–1199, https://doi.org/10.1126/science.aau5153.

Harðardóttir, S., and Coauthors,: Seasonal oceanography of Hvalfjörður in southwest Iceland 2024-2025 - CTD data. SEANOE, accessed April 10, 2026a, https://doi.org/10.17882/110439.

——, and Coauthors,: Seasonal oceanography of Hvalfjörður in southwest Iceland 2024-2025 – discrete samples. SEANOE, accessed April 10, 2026b, https://doi.org/10.17882/110401.

——, and Coauthors,: Seasonal oceanography of Hvalfjörður in southwest Iceland 2024-2025 – mooring data. SEANOE, accessed April 10, 2026c, https://doi.org/10.17882/113246.

Heede, U., K., 2026: CWorthy-ocean/C-Star-in-Hvalfjordur: Manuscript_submission_0, https://doi.org/10.5281/zenodo.20346411.

Hersbach, H., and Coauthors, 2020: The ERA5 global reanalysis. Quarterly Journal of the Royal Meteorological Society, 146, 1999–2049, https://doi.org/10.1002/qj.3803.

https://doi.org/10.5194/egusphere-2026-2920
Preprint. Discussion started: 12 June 2026

Ho, D. T., and L. Bopp, 2024: Marine carbon dioxide removal may be a future climate solution. Dialogues on Climate Change, 1, 56–62, https://doi.org/10.1177/29768659241293223.

Ho, D. T., P. Schlosser, and T. Caplow, 2002: Determination of Longitudinal Dispersion Coefficient and Net Advection in the Tidal Hudson River with a Large-Scale, High Resolution SF6 Tracer Release Experiment. Environ. Sci. Technol., 36, 3234–3241, https://doi.org/10.1021/es015814+.

Huang, Y., A. Tagliabue, and N. Cassar, 2022: Data-driven modeling of dissolved iron in the global ocean. Frontiers in Marine Science, 9, 837183.

Icelandic Meteorological Office,: Grundartangi weather station dataset subset. Accessed April 10, 2026, https://vedur.mogt.is/harbor/index.php?action=ReadingsDrillDown&harborid=1&stationid=1002&getlist=1#.

He, J. Isometric and [C]Worthy partner to advance marine carbon dioxide removal research,. Accessed February 27, 2026a, https://isometric.com/writing-articles/isometric-and-c-worthy-partner-to-advance-marine-carbon-dioxide-removal-research.

Jean-Michel, L., and Coauthors, 2021: The Copernicus Global 1/12° Oceanic and Sea Ice GLORYS12 Reanalysis. Front. Earth Sci., 9, https://doi.org/10.3389/feart.2021.698876.

Kok, J. F., and Coauthors, 2020: Improved representation of the global dust cycle using observational constraints on dust properties and abundance. Atmospheric Chemistry and Physics Discussions, 2020, 1–45.

Landschützer, P., N. Gruber, and D. C. E. Bakker, 2016: Decadal variations and trends of the global ocean carbon sink. Global Biogeochemical Cycles, 30, 1396–1417, https://doi.org/10.1002/2015GB005359.

Laurent, A., B. Wang, D. Atamanchuk, S. Rakshit, K. Azetsu-Scott, C. Algar, and K. Fennel, 2026: A high-resolution nested model to study the effects of alkalinity additions in Halifax Harbour, a mid-latitude coastal fjord. Biogeosciences, 23, 115–135, https://doi.org/10.5194/bg-23-115-2026.

Lewis, E., D. Wallace, and L. J. Allison, 1998: Program developed for CO {sub 2} system calculations. Brookhaven National Lab., Dept. of Applied Science, Upton, NY (United States …, accessed April 10, 2026, https://www.osti.gov/biblio/639712.

https://doi.org/10.5194/egusphere-2026-2920
Preprint. Discussion started: 12 June 2026

Lippiatt, S.,: Building the Integrity Infrastructure for mCDR Modeling. [C]Worthy. Accessed February 27, 2026, https://www.cworthy.org/blog/building-the-integrity-infrastructure-for-mcdr-modeling.

Liu, F., U. Daewel, J. Kossack, K. T. Demir, H. Thomas, and C. Schrum, 2025: Evaluating ocean alkalinity enhancement as a carbon dioxide removal strategy in the North Sea. Biogeosciences, 22, 3699–3719, https://doi.org/10.5194/bg-22-3699-2025.

Long, M. C., and Coauthors, 2021: Simulations With the Marine Biogeochemistry Library (MARBL). J Adv Model Earth Syst, 13, e2021MS002647, https://doi.org/10.1029/2021MS002647.

Loose, N., 2026: ROMS-Tools: Reproducible Preprocessing and Analysis for Regional Ocean Modeling with ROMS. Submitted to Journal of Open-Source Software. Preprint: https://github.com/CWorthy-ocean/roms-tools/blob/main/paper.pdf

Macrander, A., Sólveig R. Ólafsdóttir, Magnús Danielsen, Hjalti Karlsson, Arnþór Bragi Kristjánsson, and Jacek Sliwinski, 2021: Arnarfjörður: Ástand sjávar, straumar og endurnýjun botnlags / Arnarfjörður: Hydrographic conditions, currents and renewal of bottom layer. HV 2021-38. Hafrannsóknastofnun, accessed April 7, 2026, https://www.hafogvatn.is/static/research/files/hv2021-38.pdf.

Middelburg, J. J., K. Soetaert, and M. Hagens, 2020: Ocean Alkalinity, Buffering and Biogeochemical Processes. Reviews of Geophysics, 58, e2019RG000681, https://doi.org/10.1029/2019RG000681.

Olsen, A., and Coauthors, 2016: The Global Ocean Data Analysis Project version 2 (GLODAPv2) – an internally consistent data product for the world ocean. Earth System Science Data, 8, 297–323, https://doi.org/10.5194/essd-8-297-2016.

OpenTopography, 2020: Global Bathymetry and Topography at 15 Arc Sec: SRTM15+ V2.5.5.

Paul, A. J., M. Haunost, S. U. Goldenberg, J. Hartmann, N. Sánchez, J. Schneider, N. Suitner, and U. Riebesell, 2025: Ocean alkalinity enhancement in an open-ocean ecosystem: biogeochemical responses and carbon storage durability. Biogeosciences, 22, 2749–2766, https://doi.org/10.5194/bg-22-2749-2025.

Sarmiento, J. L., and N. Gruber, 2006: Ocean biogeochemical dynamics. Princeton University Press 503pp.

Shchepetkin, A. F., and J. C. McWilliams, 2005: The regional oceanic modeling system (ROMS): a split-explicit, free-surface, topography-following-coordinate oceanic model. Ocean Modelling, 9, 347–404, https://doi.org/10.1016/j.ocemod.2004.08.002.

https://doi.org/10.5194/egusphere-2026-2920
Preprint. Discussion started: 12 June 2026

Welcome to the C-Star Documentation! — C-Star documentation,. Accessed February 27, 2026b, https://c-star.readthedocs.io/en/latest/index.html.

Yankovsky, E., M. Zhou, M. Tyka, S. Bachman, D. T. Ho, A. Karspeck, and M. C. Long, 2025: Impulse response functions as a framework for quantifying ocean-based carbon dioxide removal. Biogeosciences, 22, 5723–5739, https://doi.org/10.5194/bg-22-5723-2025.

Zhou, M., M. D. Tyka, D. T. Ho, E. Yankovsky, S. Bachman, T. Nicholas, A. R. Karspeck, and M. C. Long, 2025: Mapping the global variation in the efficiency of ocean alkalinity enhancement for carbon dioxide removal. Nat. Clim. Chang., 15, 59–65, https://doi.org/10.1038/s41558-024-02179-9.

Zweng, M. M., and Coauthors,: NOAA Atlas NESDIS 61.